



Hydrometeorology and hydrology of flooding in Cape Fear River basin during Hurricane Florence in 2018



Dongxiao Yin ^a, Z. George Xue ^{a,b,c,*}, John C. Warner ^d, Daoyang Bao ^a, Yongjie Huang ^e, Wei Yu ^f

^a Department of Oceanography and Coastal Sciences, Louisiana State University, Baton Rouge, LA 70803, USA

^b Center for Computation and Technology, Louisiana State University, Baton Rouge, LA 70803, USA

^c Coastal Studies Institute, Louisiana State University, Baton Rouge, LA 70803, USA

^d U.S. Geological Survey, Woods Hole Coastal and Marine Science Center, Woods Hole, MA 02543, USA

^e Center for Analysis and Prediction of Storms, University of Oklahoma, Norman, OK 73072, USA

^f Weather Tech, LLC, Weather Tech Services, LLC, Longmont, CO 80503, USA

ARTICLE INFO

Keywords:

Hurricane Florence
Flood hydrology
Hydrometeorology
Cape Fear River Basin
WRF-Hydro

ABSTRACT

Hurricanes are the major flood generating mechanism dominating the upper tail of the peak discharge distribution over the Cape Fear River Basin (CFRB). In 2018, Hurricane Florence swamped CFRB as the ninth-most-destructive hurricane ever hit the United States and set new records of peak discharges over the main river channel and three out of five of its major tributaries. In this study, we examined the hydrometeorology and hydrology of this flood via combined observation and numerical experiment analyses. Our results suggest that the slow-motion in combination to the "L-shaped" path was the most distinctive feature of the hurricane that incurred catastrophic and widespread rainfall and flooding over CFRB. The total rainfall from the storm played a controlling role in the magnitude and spatial distribution of the flood peaks at basin scale. Above that, the spatial heterogeneities of rainfall distribution and hydrologic characteristics was responsible for the distinctive flood responses within the basin. The bi-peak shape of the flood hydrograph for the Deep River was due to the combined effects of rainfall distribution, land cover, and topographic gradient. The exceptional unit peak discharge over the Black River basin was associated with its drainage network structure, topographic gradient and rainfall distribution. The floodplain downstream of the Cape Fear River temporarily stored flood water and attenuated both the riverine floods from upstream and the compound flood over the coastal area. Furthermore, numerical analyses found that re-infiltration accounted for 76% of the total infiltration on average. Re-infiltration was superior to local infiltration over CFRB during Hurricane Florence.

1. Introduction

Landfalling tropical cyclones are a major cause of inland floods over the eastern United States (Smith et al., 2010; Villarini et al., 2014; Villarini and Smith, 2010). From 1963 to 2012, the inland flooding and associated mudslides induced by hurricanes accounted for 628 deaths (Rappaport, 2014). For the past 3 decades, 43 inland flooding events have caused an annual average of \$8.2 billion in damage. Despite this substantial human and economic loss, compared with coastal damages, relatively little effort has been devoted to study tropical cyclone induced inland flooding (Villarini et al., 2014). The limited number of published researches have pointed out the influence of meteorological factors including spatial rainfall distribution (Smith et al., 2010; Villarini et al., 2011), short-term rainfall intensity (Smith et al., 2005), hurricane track

(Huang et al., 2012; Li et al., 2020) as well as translation speed and direction (Sturdevant-Rees et al., 2001), antecedent soil condition (Chen et al., 2015; Li et al., 2020), land surface characteristics such as land use/cover (Li et al., 2020; Zhang et al., 2018), drainage network (Smith et al., 2005; Sturdevant-Rees et al., 2001) and topography (Smith et al., 2005; Sturdevant-Rees et al., 2001; Villarini et al., 2011) on the flood response.

The Cape Fear River Basin (CFRB) is located in the east-central North Carolina, U.S. Hurricanes dominate the upper tail of peak discharge distributions in the basin (Fig. 1a). The top ten maximum unit peak discharges over the Cape Fear River and its five major tributaries were all induced by hurricanes (Fig. 1b). Among them, Hurricane Florence (Florence) stands out as the most powerful flood-generating event with more widespread and significant influence than the others. During Florence, peak discharge records were set over the Cape Fear River and

* Corresponding author at: Department of Oceanography and Coastal Sciences, Louisiana State University, Baton Rouge, LA 70803, USA.

E-mail address: zxue@lsu.edu (Z.G. Xue).

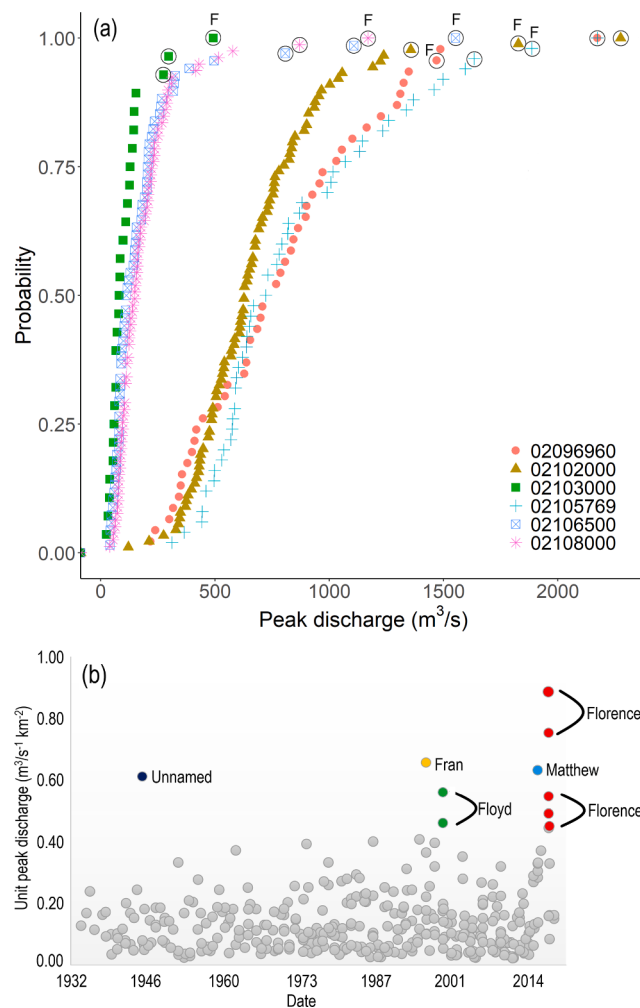


Fig. 1. (a) Accumulative probability curve of annual peak discharges for the Haw River at Bynum (02096960), the Deep River at Moncure (02102000), the Little River at Manchester (02103000), the Black River at Tomahawk (02106500), the Northeast Cape Fear River at Chinquapin (02108000) and the Cape Fear River at Kelly (02105769). The circled symbols indicate that the peak discharge ranks top three among the records and is induced by hurricane events. “F” represents the peak discharge caused by Florence. Note that small peak discharges associated with hurricanes are not labeled. The locations of the gages are shown in Fig. 2b. (b) Annual unit peak discharges for the Cape Fear River and its five major tributaries based on available observation data at the six USGS gages in (a). The top ten peaks are marked out from the others with separate colors.

three out of its five major tributaries. Three U.S. Geological Survey (USGS) gages recorded peak discharges with return intervals equal to or larger than a 500-year flood event (Table 1).

Recent studies have assessed the extremeness of Florence induced rainfall (Kunkel and Champion, 2019) and the principal causes behind it (Callaghan, 2020). The flood induced by Florence over the coastal area has been investigated using numerical model (Gori et al., 2020) and observational data (Griffin et al., 2020; Williams et al., 2020). In addition, Florence was also investigated to evaluate a newly proposed data assimilation method (Gharamti et al., 2021), to explore the benefit of applying crowdsourced data (Hultquist and Cervone, 2020) in flood mapping, and to demonstrate the importance of an accurate representation of ocean state (Zambon et al., 2021) in hurricane simulation. Nevertheless, characteristics of the inland flooding and the controlling mechanism behind it has not been investigated yet.

The primary objective of this study is to identify the hydrometeorological and hydrological controls of the extreme inland flooding

Table 1

Observed peak discharge and the recurrence interval over the Cape Fear River and its five major tributaries during Florence.

River	Number of annual peak discharge in record	Peak discharge (m³/s)	Ranking ^a	Recurrence interval (year) (Feaster et al., 2018)
Haw River	46	1470	3	–
Deep River	89	1826	2	–
Little River	28	493	1	500
Black River	68	1552	1	>500
Northeast Cape Fear River	79	1169	1	>500
Cape Fear River	50	2172	1	67

a: With regards to historical peak discharges recorded at the corresponding USGS gages shown in Fig. 1a.

caused by Florence. We analyzed the precipitation based on the Stage IV Quantitative Precipitation Estimate (QPE) product (Lin, 2011) and investigated the flood hydrology with streamflow observations. In addition, we analyzed the results of a well calibrated Weather Research and Forecasting Model Hydrological modeling extension package (WRF-Hydro) model to gain an insight into the significance of the re-infiltration process during Florence. The rest of the paper is organized as follows. Section 2 describes the study region and method. Section 3 presents the precipitation analysis. In Section 4, flood response is analyzed, and its controlling mechanism is discussed. The paper is closed with a summary and conclusions in Section 5.

2. Study region and methodology

2.1. Cape Fear River basin

As the largest river basin contained entirely within the borders of North Carolina, CFRB has a drainage area of 23,889 km². Inside the basin, the elevation ranges from 364 m in the headwater region to nearly 0 m over the coastal plain area. The CFRB contains five major sub-basins (Fig. 2b), which are the Haw River and the Deep River basin upstream, the Little River basin in the middle, and the Northeast Cape Fear River and Black River basin downstream. The Haw River and Deep River basin contains two USGS HUC-8 units-HUC 03030002 and HUC 03030003 (Fig. 2d) and features a rolling and hilly landscape. The Little River basin is within the middle CFRB (HUC 03030003) and is characterized by rolling terrain with little relief. The lower CFRB is composed of 3 USGS HUC-8 units (HUC 03030005-07, Fig. 2d) and is drained by the main stem of Cape Fear River, Black River, and Northeast Cape Fear River from west to east, respectively. The topography in the lower part of CFRB is characterized by low elevation and minimum topographic gradient.

From 1996 to 2018, 13 hurricanes have made landfalls in the basin or passed by within 120 km from it. Six hurricanes have caused significant flood damages (Gori et al., 2020). A recent study suggests a regime shift in coastal North Carolina towards increasingly high precipitation associated with tropical cyclones (Paarl et al., 2019). In addition, CFRB is the most industrialized watershed in North Carolina with large industries and dozens of big cities sitting within its boundaries.

The CFRB involves intensive water management activities. There are around 1,100 impoundments with dams spread over the basin, the majority of which are in the upper part (Curtis Weaver et al., 2001). Among them, the B. Everett Jordan Lake (Jordan Lake hereafter, Fig. 2b) is the largest surface area impoundment covering an area of 56.4 km². Located 7 km upstream of the mouth of the Haw River, Jordan Lake Dam is able to retain the runoff from the drainage area from a six-inch rainfall (N. C. Department of Environmental Quality Division of Water Resources, 2016). Along the Deep River and the mainstream of Cape Fear

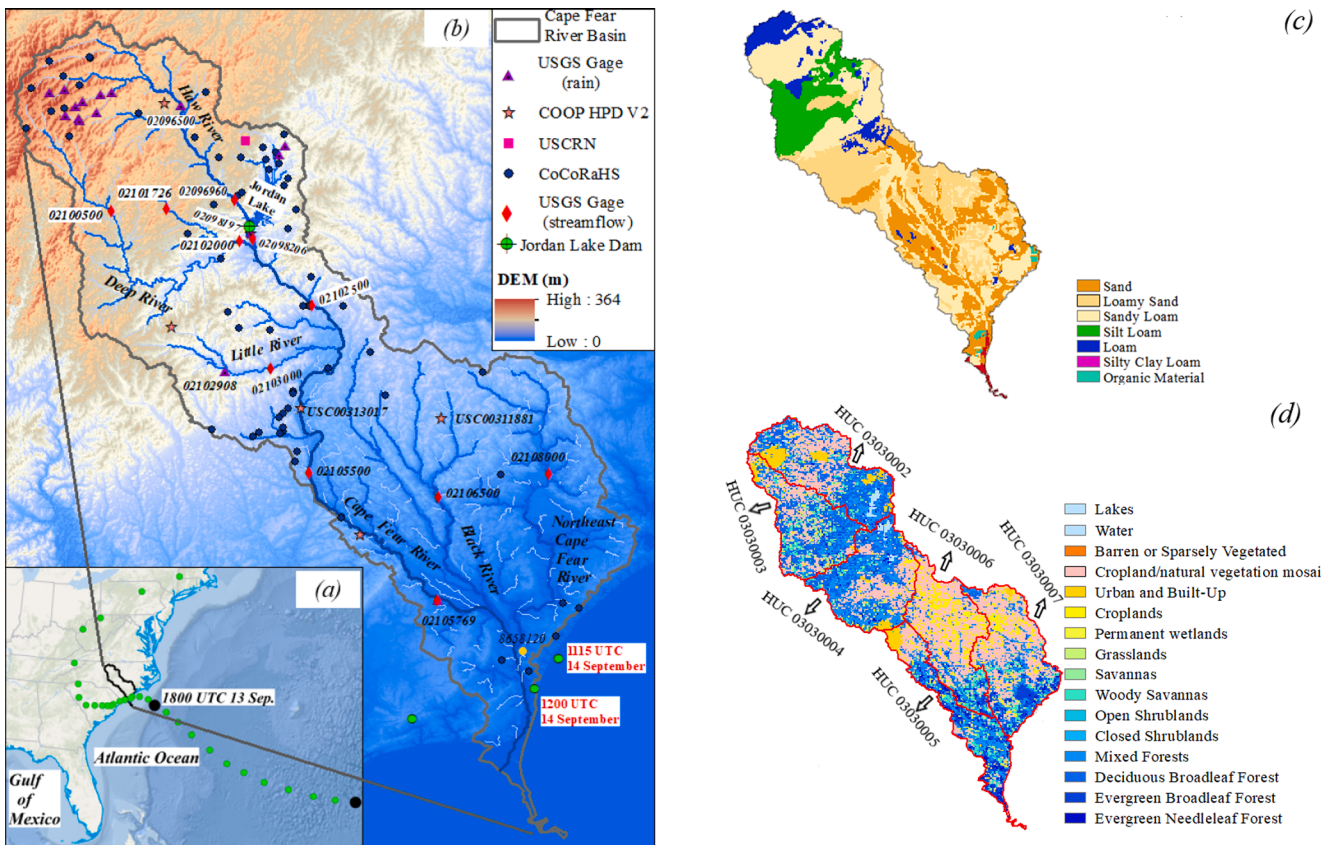


Fig. 2. (a) NOAA best track for Hurricane Florence with 6 h interval. The CFRB is outlined with a solid black line. (b) Topography, river network, Rain gages (COOP HPDV2, USCRN, CoCoRaHS, USGS Rain Gages), NOAA tidal gage station (8658120), USGS Streamflow Gages and Jordan Lake Dam. The NOAA best track for Hurricane Florence with 6 h interval is also presented with solid green circles. (c) Soil type over the CFRB. (d) Land-use type over the CFRB. USGS HUC 8 watersheds are outlined with solid red lines with identification numbers labeled. (For interpretation of the references to colour in this figure legend, the reader is referred to the web version of this article.)

River, there is also a series of small dams. Those dams are typically operated on the basis of “run-of-river” mode in which outflows from them are almost equal to inflows (Weaver and Carolina, 1997).

According to the 21 Category Modified International Geosphere-Biosphere Programme (IGBP) Moderate Resolution Imaging Spectrometer (MODIS) land cover product, there are 16 types of land cover over the CFRB. The dominant land use types are cropland/natural vegetation mosaic (32%), mixed forests (20%), deciduous broadleaf forest (18%). Besides that, Croplands and Urban/Built-up account for 6.8% and 3.5% over the whole basin, respectively. The soil types are mainly sandy loam (33.6%), loamy sand (24.2%), sand (22.1%), silt loam (11.9%), and loam (7.1%) according to the State Soil Geographic Database (Miller and White, 1998).

2.2. Methodology

Our analysis was performed based on both observation and numerical simulation. Observation data used are detailed in Table 2 and Table 3, which include three QPE products, rain gage observations, streamflow observations, and annual peak discharges. Numerical simulations were conducted using WRF-Hydro (Gochis et al., 2020), which is detailed in Section 4.4.

It should be noted that the QPE products were evaluated against the rain gage observations prior to formal analysis. A point-to-grid (rain gage-to-QPE) comparison over storm total rainfall and hourly rainfall intensity following previous studies (Cánoyas-García et al., 2018; Thiemig et al., 2012; Zambrano-Bigarini et al., 2017) was carried out. Here, storm total rainfall refers to the accumulated precipitation from 0000 UTC 14 to 0000 UTC 18 September 2018. The modified Kling-

Table 2
Overview of the data used in this study.

Variable	Source	Time interval	Spatial resolution	No. Gages/Data Points
QPE rainfall	NLDAS V2 ^a	Hourly	1/8 Degree	–
	Stage IV ^b	Hourly	4 km	–
	MRMS ^c	Hourly	1 km	–
Rain gage observations	CoCoRaHS ^d	Daily	–	62/62
	COOP HPD V2 ^e	Hourly	–	6/558
	USCRN ^f	Hourly	–	1/96
	USGS ^g	5/15-min	–	17/1564
Streamflow	USGS	15–60-min	–	–
Annual peak discharge	USGS	–	–	6

a: The precipitation field embedded in Phase 2 of the North American Land Data Assimilation System (Mitchell et al., 2004; Xia et al., 2012).

b: The Stage IV multi-sensor rainfall estimation product produced by the National Centers for Environmental Prediction (NCEP) in the United States (Lin, 2011).

c: The Multi-Radar Multi-Sensor system was developed at the National Severe Storm Laboratory and the University of Oklahoma (Zhang et al., 2016).

d: The Community Collaborative Rain, Hail and Snow Network.

e: The Cooperative Observer Program Hourly Precipitation Data, Version 2.

f: The United States Climate Reference Network (USCRN, hourly).

g: The United States Geological Survey.

Table 3

Name, drainage basin, identification number, and drainage area of USGS Gages.

Name	Drainage basin	USGS Gage	Drainage area (km ²)
Bynum	Haw River	02096960	3302
Moncure	Jordan Lake Dam	02098206	4380
Moncure	Deep River	02102000	3714
Ramseur		02100500	904
Siler City		02101726	178
Manchester	Little River	02103000	901
Tomahawk	Black River	02106500	1751
Chinquapin	Northeast Cape Fear River	02108000	1551
Lillington	Cape Fear River	02102500	8972
Tar heel		02105500	12,567
Kelly		02105769	13,610

Gupta Efficiency (KGE, Eq.(1), Gupta et al., 2009; Zambrano-Bigiarini et al., 2017) was calculated to quantitatively measure the overall agreement between estimates and rain gage observations.

The calculation of KGE (Eq.(1)) involves three independent components: Pearson correlation coefficient (γ , Eq.(2)), relative bias (α , Eq.(3)) and variability term (β , Eq.(4)), which can be used to assess the skill of QPEs in reproducing the temporal variation, average intensity and distribution of the observed rainfall, respectively. The optimal value of KGE is 1, with a higher value indicating better performance. γ ranges from 0 to 1, with 0 representing the absence of linear correlation between estimation and observation. $\alpha > 1$ implies an overall overestimation while $\alpha < 1$ represents underestimation. Similarly, β can be used to investigate whether the variability of estimation is larger or smaller than observation.

$$KGE = 1 - \sqrt{(\gamma - 1)^2 + (\alpha - 1)^2 + (\beta - 1)^2} \quad (1)$$

$$\gamma = \frac{\sum_1^N (X_{\text{estimation}} - \mu_{\text{estimation}})(X_{\text{obs}} - \mu_{\text{obs}})}{\sqrt{\sum_1^N (X_{\text{estimation}} - \mu_{\text{estimation}})^2 * \sum_1^N (X_{\text{obs}} - \mu_{\text{obs}})^2}} \quad (2)$$

$$\alpha = \frac{\mu_{\text{estimation}}}{\mu_{\text{obs}}} \quad (3)$$

$$\beta = \frac{\sigma_{\text{estimation}}}{\sigma_{\text{obs}}} \quad (4)$$

where N represents the total number of data points, $X_{\text{estimation}}$ and X_{obs} denote the rainfall estimation from QPE products and rain gage observation, respectively, $\mu_{\text{estimation}}$ and μ_{obs} are the mean values of rainfall estimation and observation, $\sigma_{\text{estimation}}$ and σ_{obs} stand for the standard deviations of estimation and observation, respectively.

3. Hydrometeorological analysis of Florence

3.1. QPE evaluation

Table 4 and Fig. 3 summarize the performance of the three QPE products in reproducing the storm total rainfall (mm) and hourly rainfall intensity (mm/h) during Florence.

All three QPEs can satisfactorily capture the storm total rainfall with KGE larger than 0.7. Stage IV appears to be the “best” product with the

Table 4

Statistical performances of point-to-grid comparison between QPE and rain gage observations.

QPE Product	Storm total rainfall (mm)				Hourly rainfall intensity (mm/h)			
	α	β	γ	KGE	α	β	γ	KGE
NLDAS V2	0.91	0.83	0.85	0.75	0.99	0.84	0.77	0.71
Stage IV	0.85	1.07	0.91	0.82	0.88	1.13	0.85	0.77
MRMS	0.91	0.82	0.86	0.76	0.96	1.13	0.80	0.76

highest KGE (0.82) and closest-to-one β and γ . Besides, all three QPEs underestimated the storm total rainfall with α less than 1. As shown in Fig. 3a, a consistent underestimation is observed over Stage IV reproduced rainfall, while MRMS and NLDAS V2 both overestimate low values (<220 mm) and underestimate high ones (>220 mm).

Similarly, the QPEs all tend to be able to provide reasonable hourly rainfall intensity with satisfactory KGE values (larger than 0.7). Here, Stage IV and MRMS present comparable skills with KGE 0.77 and 0.76, respectively, which are better than NLDAS V2 (0.71). While Stage IV shows better performance in capturing the temporal variation of rainfall intensity with a higher γ (0.85) value than that of MRMS (0.80), the latter ($\alpha = 0.96$) is superior to the former ($\alpha = 0.88$) in reproducing the average rainfall intensity. Based on the evaluation, we consider Stage IV as the “best” QPE product for reproducing the rainfall over CFRB during Florence. The following precipitation analysis and numerical simulation are thus based on Stage IV.

3.2. Precipitation analysis

Florence made landfall as a Category 1 hurricane near Wrightsville Beach, North Carolina around 1115 UTC 14 September 2018 (Fig. 4a). It then moved towards the southwest along the coastal area and degraded into a tropical storm by 0000 UTC 15 September. Another 12 h later, the system turned westward and moved slowly across South Carolina for an additional 24 h. By 1800 UTC 16 September, it degraded into a tropical depression. From then on, the storm accelerated towards the north and became extratropical by 1200 UTC on 17 September. Finally, it dissipated around 1800 UTC the next day.

Florence was a slow-moving system prior to and immediately after landfall. The forward speed ranged from 3.6–14.4 km/h during 14–16 September (Kunkel and Champion, 2019). This sluggish speed led to torrential rainfall accumulation over the lower CFRB. In addition, Florence followed a unique track. As shown in Fig. 4a, major hurricanes impacting CFRB such as Fran (1996), Floyd (1999), and Matthew (2016) followed a relatively constant direction before and after passing over CFRB. By contrast, Florence showed an “L-shaped” path. As it tracked along the path, its rainbands extended into different parts of CFRB from the coastal plain to the headwater area as discussed right below and summarized in Table S1. The combination of the slow storm motion and the unique track was the distinctive hydrometeorological feature of Florence that contributed to the widespread flood response over the entire CFRB. Fig. 4b compares the storm total rainfall associated with the four most disastrous hurricanes impacting CFRB. The storm total rainfall induced by Florence is the highest among all four major hurricanes over not only the major basin but also each sub-basin. This tremendous amount of rainfall laid the foundation for the widespread and extreme flood, with which other hurricane events cannot compete.

In addition, with Stage IV QPE and rain gage observations, we present the spatiotemporal evolution of the rainfall distribution and its influence on rainfall intensity across the basin. Following the method of Jiang et al. (2013), the rainfall fields associated with Florence at different stages were categorized into the inner core region, the inner rainband region, and the outer rainband region. The inner core region includes eyewalls when the storm has a discernible eye. Immediately adjacent to inner core region is the inner rainband, which extends outward for about 100 km. The outer rainband locates approximately 150–200 km from the center of the storm and extends to the farthest rainfall element.

The rainband of Florence approached CFRB around 0000 UTC on 14 September (Fig. 5a). As a result of its path, precipitation was initially measured by a rain gage over the lower part of CFRB (Fig. 6b). Florence was a Category 2 hurricane by that time, the eye of which was approximately 100 km from the land. The inner core and inner rainband were well developed and were mainly located over the right front quadrant. This rainband distribution resulted in an asymmetric rainfall structure. Eight hours later, a thin inner rainband reached the

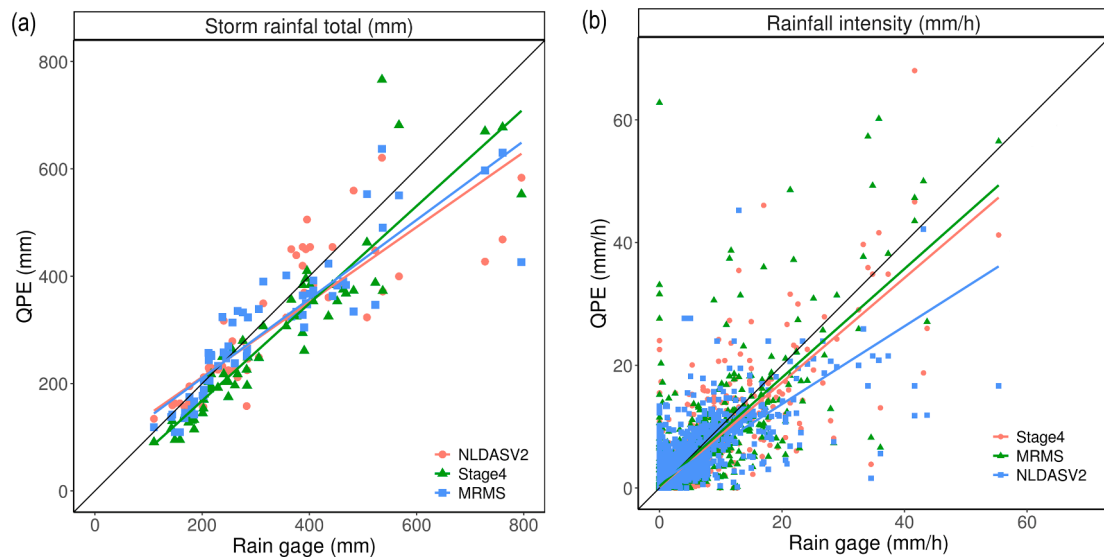


Fig. 3. Scatterplot for storm total rainfall (a) and hourly rainfall intensity (b) between rain gage observations (x-axis) and QPE estimations (y-axis). The 1:1 line (black) and linear-regression lines are also shown. Statistical performances are shown in Table 4.

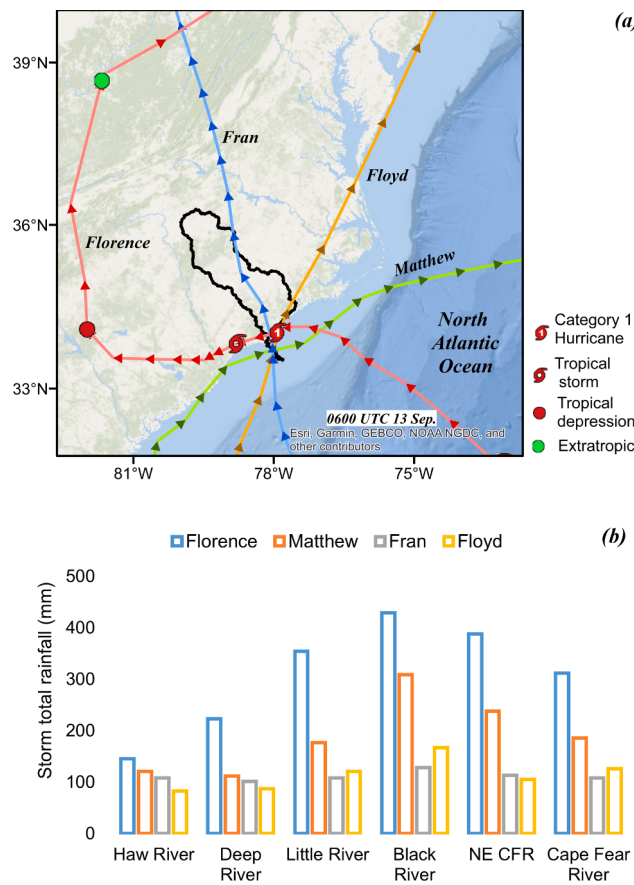


Fig. 4. (a) NOAA best track for Hurricane Florence (red line) with 6 h interval. The time when Florence became a Category 1 hurricane, tropical storm, tropical depression, and extratropical are marked with different symbols. The tracks of Hurricane Fran (blue line), Floyd (brown line), and Matthew (green line) are also shown. For reference, CFRB is outlined in a solid black line. (b) Storm total rainfall over CFRB during the four most disastrous hurricane events. The storm total rainfall was calculated based on the NLDAS V2 product due to the lack of Stage IV product before 2002. (For interpretation of the references to colour in this figure legend, the reader is referred to the web version of this article.)

downstream part of the lower CFRB (Fig. 5b). This rainband was responsible for the first pulse of heavy rainfall (rainfall rate greater than 10 mm/h, Fig. 6a). At 1100 UTC 14 September, Florence made landfall (Fig. 5c) and started cresting across the lower CFRB. Meanwhile, the rain area of Florence broadened. The inner core and inner rainband controlled the rainfall over the lower CFRB until 1500 UTC 14 September when the inner core moved out of CFRB (Fig. 5d), marking the end of the first pulse of rainfall (Fig. 6a-b). Since then, inner and outer rainbands took over as the major rainfall agent for the lower CFRB. By 0900 UTC 15 September, the largest rainfall rate from the storm occurred due to strong convection from an inner rainband that extended along the mainstem of the Cape Fear River (see Fig. 5e). Maximum rainfall rates observed at USGS gage 02105769 (Fig. 6a) and COOP HPD V2 gage USC00311881 (Fig. 6b) were 33.3 mm/h and 43.7 mm/h, respectively. Florence degraded into a tropical storm (Fig. 5g) and lost its distinguishable rainfall structure at 1800 UTC 16 September. Afterward, the system accelerated northward and the lower CFRB became out of reach from the rainbands, after which little rainfall was observed. Thus, the period of rainfall was mainly from 0000 UTC 14 to 18,000 UTC 16 September for 67 h over the lower CFRB. During this period, 88% of 500 mm storm total rainfall over the reach between Tarheel (02105500) and Kelly (02105769) along the Cape Fear River was dumped. 85% and 95% of the 411 mm and 512 mm storm total rainfall over the Black River basin above Tomahawk (02106500) and Northeast Cape Fear River basin above Chinquapin (02108000) were accumulated, respectively.

Over the middle CFRB where the Little River basin resides, the first pulse of rainfall (Fig. 6c-6d) commenced as an outer rainband arrived at 1500 UTC 14 September (Fig. 5d). From then on till 0800 UTC 17 September (Fig. 5h), rainfall over this area was controlled by the outer rainband of Florence. Following the movement of the storm, the middle CFRB fell in or out of the coverage of the rainband. Consequently, five pulses of rainfall were observed at the rain gages (Fig. 6c-d). During this 66-hour rainfall window, 97% of 269 mm storm total rainfall over the Little River above Manchester (02103000) was accumulated. Mean rainfall intensities were 4.0 mm/h at USGS 02102908 and 4.5 mm/h at USC00313017, respectively. And the maximum rainfall intensities were 25.1 mm/h and 34.5 mm/h, respectively, which only lasted for one hour during the last pulse.

Two pulses of rainfall were observed over the upper part of the basin (Fig. 6e-f). The first one started from 1800 UTC 14 September and lasted for 48 h until the degradation of Florence into tropical depression (Fig. 5g). During this period, rainfall was light to moderate, the

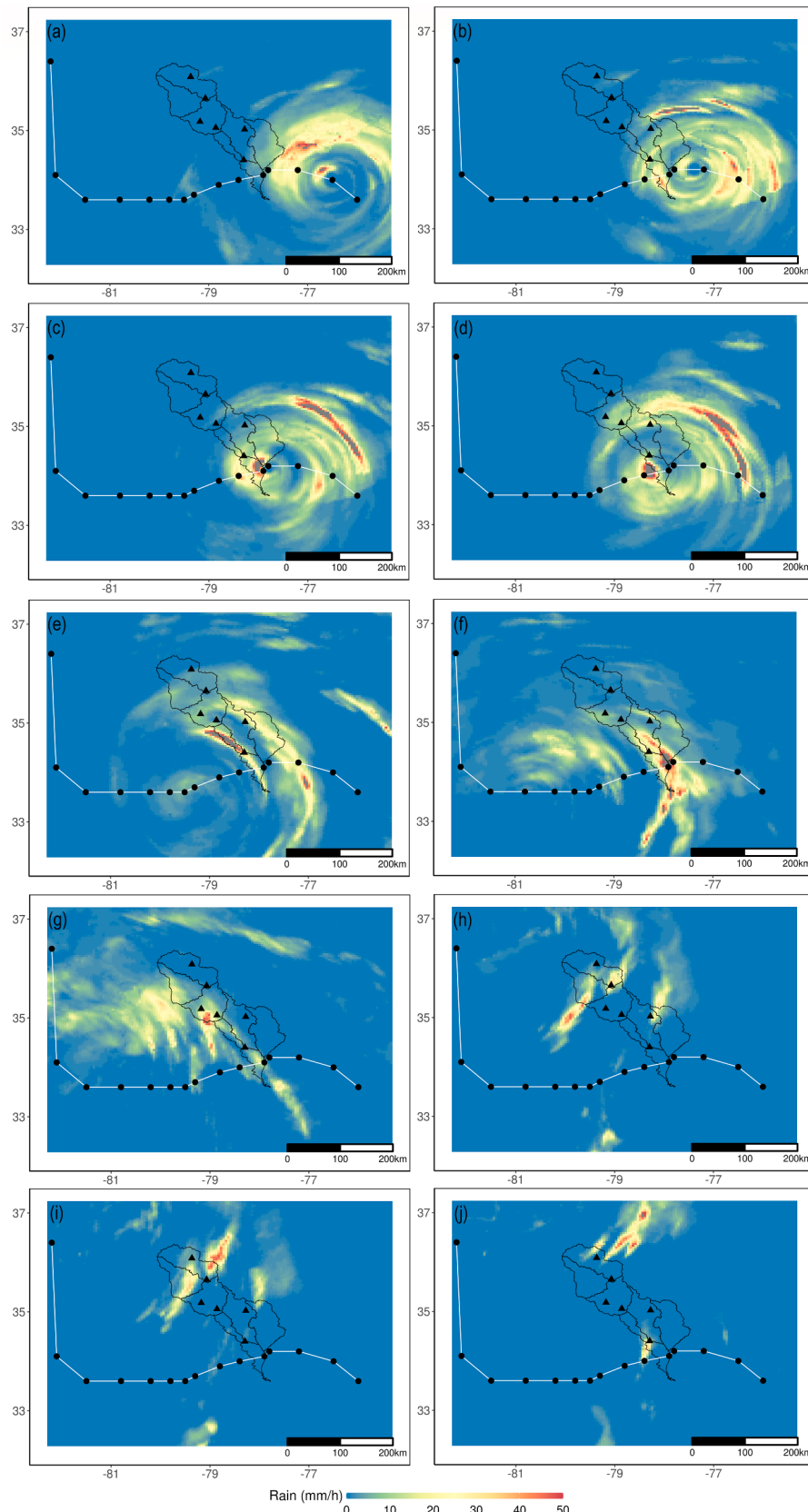


Fig. 5. Rainfall intensity (mm/h) over the CFRB during Hurricane Florence for 14 September 2018 at (a) 0000 UTC, (b) 0800 UTC, (c) 1100 UTC, (d) 1500 UTC, for 15 September 2018 at (e) 0900 UTC, for 16 September 2018 at (f) 0600 UTC and (g) 1800 UTC, for 17 September 2018 at (h) 0800 UTC, at (i) 1000 UTC and at (j) 1300 UTC. The black triangles represent rain gages shown in Fig. 6. From upstream to downstream, they are USGS gage 02096500, USGS gage 02098197, USGS gage 02102908, USC00313017, USC00311881 and USGS gage 02105769, respectively. The NOAA best track for Hurricane Florence with 6 h interval is shown with a white line. The 6 USGS HUC 8 watersheds are outlined with solid grey lines.

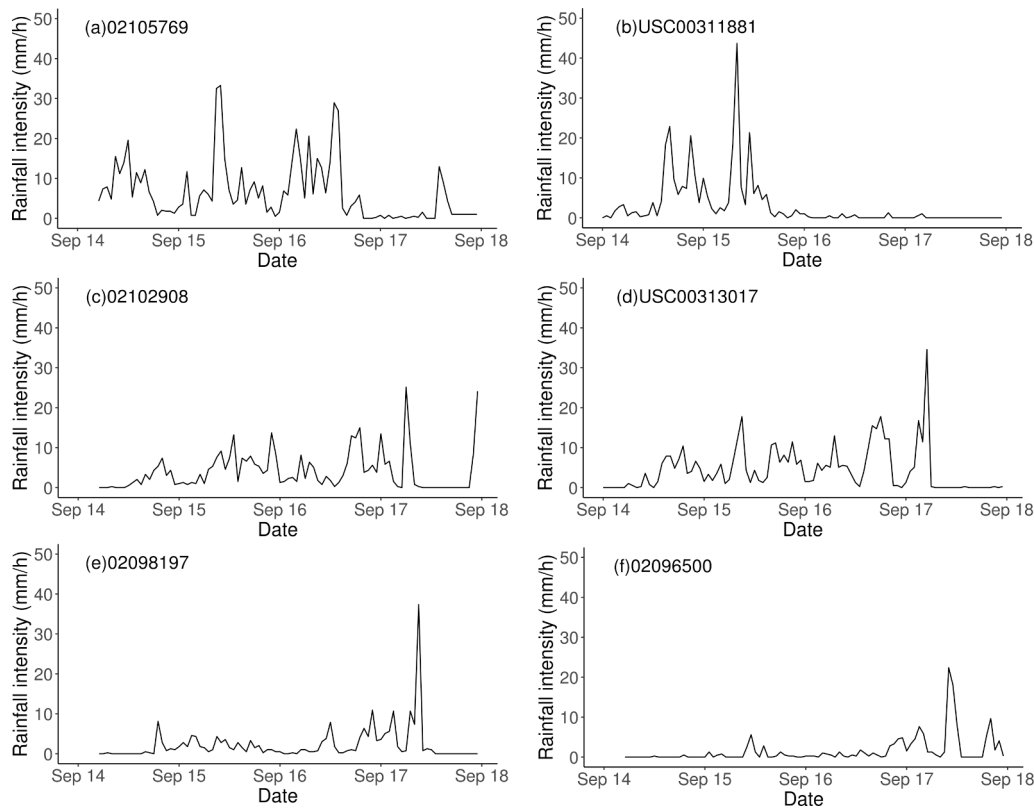


Fig. 6. Time series of rain gage observations with 1 h interval (a) USGS gage 02105769, (b) USC00311881, (c) USGS gage 02102908, (d) USC00313017, (e) USGS gage 02098197 and (f) USGS gage 02096500. See Fig. 2b and Fig. 5 for gage locations.

accumulative rainfall over Haw River basin above Bynum (02096960) and Deep River basin above Moncure (02102000) were 29 mm and 86 mm, respectively. Mean rainfall rates were 1.8 mm/h and 0.6 mm/h and maximum rainfall rates 8.1 mm/h and 5.6 mm/h at USGS gage 02098197 (Fig. 6e) and 02096500 (Fig. 6f), respectively. Following the first pulse of rainfall, the outer rainband associated with the hurricane remnant passed over and induced rainfall for another 20 h till 1300 UTC 17 September (Fig. 5j). The second pulse of rainfall was much heavier than the first one. The accumulated rainfall over the Haw River basin above Bynum (02096960) and the Deep River basin above Moncure (02102000) during this period were 89 mm and 137 mm, respectively.

The mean rainfall rates observed at USGS gage 02098197 (Fig. 6e) and 02096500 (Fig. 6f) were 5.8 mm/h and 4.6 mm/h, respectively. The largest rainfall rate during this period occurred at 1000 UTC on 17 September (Fig. 5i) due to the intensive convection over a remnant rainband. USGS gage 02098197 (Fig. 6e) and 02096500 (Fig. 6f) observed maximum rainfall rates of 37.3 mm/h and 22.4 mm/h, respectively.

4. Flood hydrology

In this section, we analyze the flood hydrology associated with

Table 5
Summary of flood response over the Cape Fear River basin during Florence.

Basin	Station	Effective Drainage Area ^a (km ²)	Unit peak discharge (m ³ /s ⁻¹ km ⁻²)	Lag time (hour)	Runoff volume/ Peak discharge (h)	Runoff depth ^b (mm)	Rainfall (mm)	Runoff/ rainfall ^c
Haw River	Bynum (02096960)	3302	0.45	26.25	61.7	101	122	0.82
Deep River	Moncure (02102000)	3714	0.49	23.75	103.7	183	225	0.81
Little River	Manchester (02103000)	901	0.55	51	96.0	190	269	0.71
Black River	Tomahawk (02106500)	1751	0.89	64	100.0	318	411	0.78
NE CFR	Chinquapin (02108000)	1551	0.75	51.25	128.5	347	512	0.68
Jordan Lake Dam	Moncure (02098206)	4380	0.07	–	–	73	139	0.53
Mainstem of the Cape Fear River	Lillington (02102500)	4592	0.39	34	118.2	166	223	0.74
Tar heel (02105500)	8187	0.30	61.75	151.9	164	255	0.64	
Kelly (02105769)	9230	0.24	127.75	233.8	202	283	0.71	
Moncure-Lillington (02102000–02102500)	878	–	–	–	94	215	0.44	
Lillington-Tar Heel (02102500–02105500)	3595	–	–	–	161	296	0.54	
Tar heel-Kelly (02105500–02105769)	1043	–	–	–	500	503	~1	

a. The drainage area of Jordan Lake dam is subtracted from that of the gage downstream of it to eliminate the influence of flood control on flood response. b. The observed discharge at USGS gage 02098206 is subtracted from the observations downstream of it to eliminate the influence of Jordan Lake Dam. c. The ratio between runoff depth and rainfall (runoff-to-rainfall ratio).

Florence based on rainfall and streamflow observations. Table 5 summarizes the flood response to Florence in terms of unit peak discharge, runoff depth, runoff-to-rainfall ratio, lag time and runoff volume-to-peak discharge ratio (VP ratio hereafter). Unit peak discharge was observed peak discharge divided by the drainage area. Unit peak discharge and VP ratio can both be used to characterize flood response. The unit peak discharge is influenced by rainfall forcing and land surface characteristics. Lower values can be the result of either lower rainfall

input or flood attenuation related to basin characteristics or both. By contrast, the VP ratio reflects mainly the influence of basin features on flood response. It can be used to quantify the relative magnitude of peak discharge and total runoff volume. Smaller values imply higher peak discharge tendency and quicker response of the basin. Runoff depth was computed by integrating observed discharge over the period of 0000 UTC 14 September to 0000 UTC 12 October 2018 and dividing it by drainage area. Basin averaged storm total rainfall was calculated from

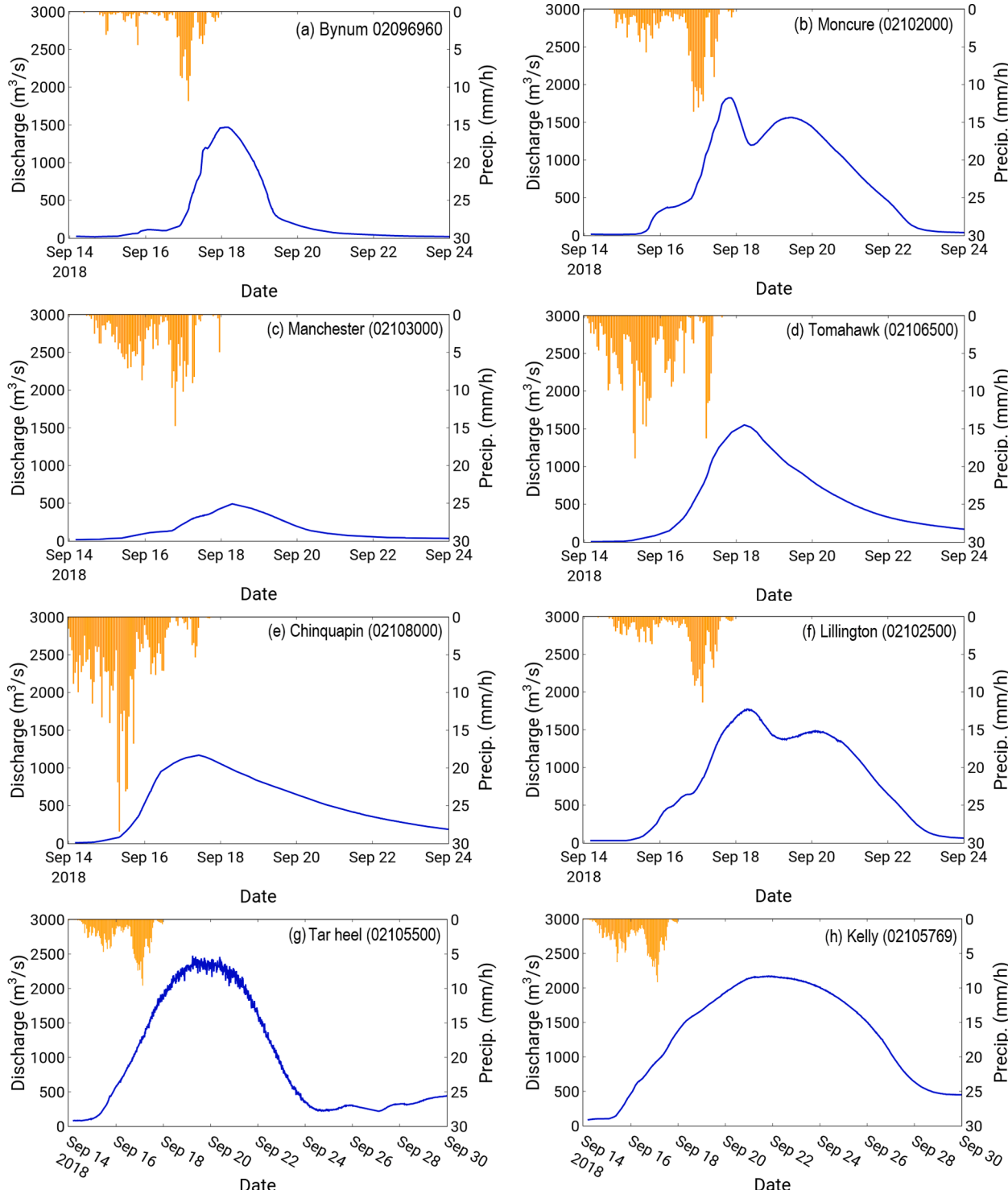


Fig. 7. Time series of areal rainfall rate and stream discharge for (a) Haw River at Bynum (02096960), (b) Deep River at Moncure (02102000), (c) Little River at Manchester (02103000), (d) Black River at Tomahawk (02106500), (e) Northeast Cape Fear River at Chinquapin (02108000) and mainstem of the Cape Fear River at (f) Lillington (02102500), (g) Tar Heel (02105500) and (h) Kelly (02105769). The locations of the gages are shown in Fig. 2b.

Stage IV QPE for the period of 0000 UTC 14 September to 0000 UTC 18 September. Lag time refers to the difference between the time of peak discharge and that at which 50% of the total rainfall occurs (Smith et al., 2000). Note that for gages downstream of Jordan Lake Dam along the main stem of the Cape Fear River, the released discharge from the dam was subtracted from the observation to exclude its effect on flood response.

4.1. Storm total rainfall over sub-river basins

Storm total rainfall was the predominant control of runoff depth over the major sub-basins. As is shown in Table 5, the runoff-to-rainfall ratio decreases from the Haw River and Deep River basins in the hilly upper CFRB to the Little River basin in the middle, and the Black River and Northeast Cape Fear River basins over the coastal region. The highest and lowest runoff-to-rainfall ratio are found in Haw River at Bynum (02096960) and Northeast Cape Fear River at Chinquapin (02108000), respectively. On the contrary, runoff depth increases from upstream to downstream over the sub-river basins, indicating the dominance of the storm total rainfall over the hydrologic characteristics in runoff production in the sub-basins.

Along the main stem of the Cape Fear River, runoff was preferentially generated over the high elevation upstream area and low elevation coastal regions. From Moncure (02102000) at the Deep River to Lillington (02102500) at the mainstem, both runoff depth and runoff-to-rainfall ratio decrease. The decreasing trend is carried on further downstream to Tar Heel (02105500). Then further downstream from Tar Heel (02105500) to Kelly (02105769), runoff depth and runoff-to-rainfall ratio increase again. This trend of runoff coefficient points out the higher flooding potential over the upper and lower CFRB than that in the middle part. As is shown in Table 5, the runoff-to-rainfall ratios over the reach from Moncure (02102000) to Lillington (02102500) and from Lillington (02102500) to Tar Heel (02105500) are 0.44 and 0.54, respectively. In sharp contrast, the ratio reaches 1 for the drainage area from Tar Heel (02105500) to Kelly (02105769).

In addition, the VP ratios are generally lower over the sub-river basins in the upper CFRB (Table 5). However, the unit peak discharges tend to follow the trend of storm total rainfall, being higher in lower CFRB. This implies the dominance of storm total rainfall in controlling the peak discharge amplitude in the sub-river basins. Further, storm total rainfall instead of peak rainfall rates was the major controller of the peak discharge distribution during Florence. Fig. 7 compares the time series of basin averaged rainfall intensity with that of the streamflow. Despite the multi-peak signature of the hyetographs, the flood hydrographs are characterized by one major peak after or right before the end of rainfall. This implies that rainfall intensity played a minimal role in influencing the peak response compared to storm total rainfall during Florence.

4.2. Land cover, topographic gradient, and flood plain storage

In this part, the timing signature of flood response is analyzed with lag time and VP ratio. As shown in Table 5, the lag times of the sub-basins over the lower and middle CFRB are two times larger than those of the Haw River and Deep River basin in the upper part. This difference is attributable to the decrease of the topographic gradient from hilly upstream to the flat coastal region in CFRB. In correspondence, the VP ratio follows a similar trend with an exception found at Moncure (02102000) over Deep River. The lag time at Moncure (02102000) is shorter than that at Bynum (02096960) (Table 5), which indicates the faster response of the Deep River basin than the Haw River basin to rainfall forcing during Florence. However, the VP ratio of the former is 68% higher than that of the latter, falling in the same magnitude with the basins downstream. This inconsistency and abnormal larger VP ratio at Moncure (02102000) is related to the bi-peak shape of the flood hydrograph (Fig. 8a).

Fig. 8a shows the nested flood hydrograph for gages along the Deep River. The initial rise of the flood hydrograph at Moncure (02102000) is attributable to the first pulse of rainfall as mentioned in Section 3 and shown in Fig. 7b. The major peak is mainly due to the downstream advection from Ramseur (02100500) and Siler City (02101726) to

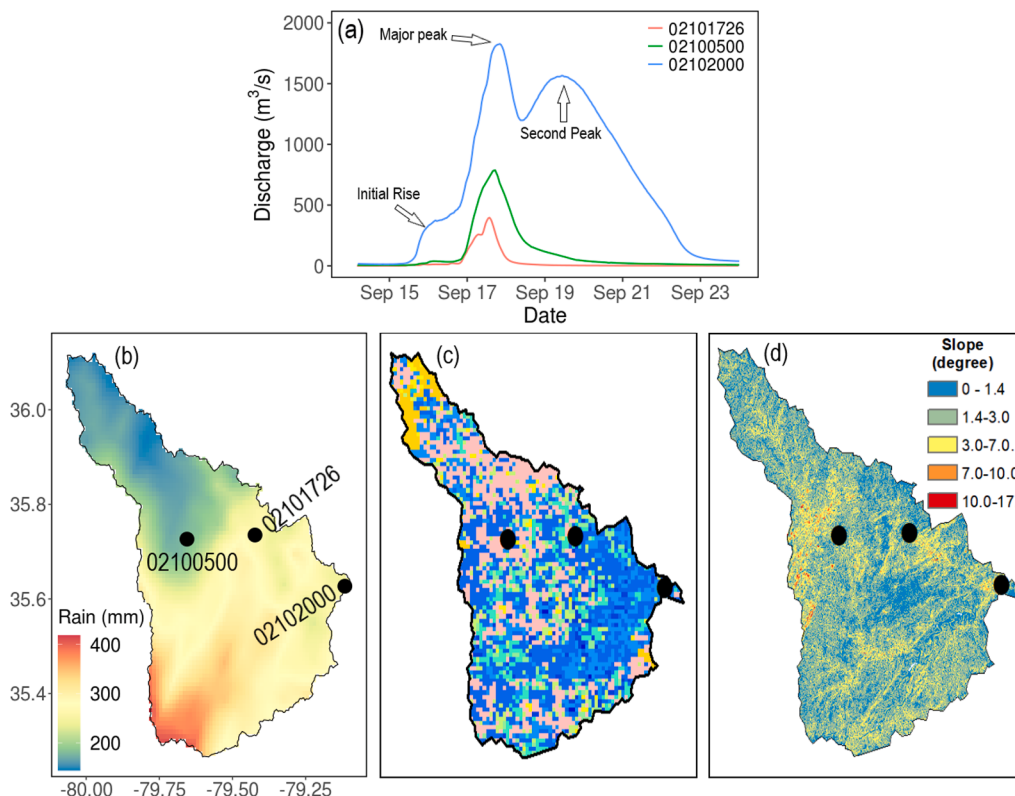


Fig. 8. (a) Nested flood hydrograph at Moncure (02102000, blue), Siler City (02101726, red) and Ramseur (02100500), (b) the storm total rainfall, (c) the land use type, and (d) topographic slope in degree over the Deep River basin. The three gages are labeled with black dots. The Deep River basin is identified in Fig. 2d as HUC 03030003. The legend of the land use type for (c) is the same as Fig. 2d. (For interpretation of the references to colour in this figure legend, the reader is referred to the web version of this article.)

Moncure. Meanwhile, the second peak is caused primarily by the advection from runoff produced over the intervening drainage area between Ramseur (02100500) and Moncure (02102000). As shown in Fig. 8b, rainfall mainly accumulated over the southwest part of Deep River basin during Florence. Here, the land cover is mainly forest (Fig. 8c), and topographic gradient is low compared to that of Ramseur (02100500) and Siler City (02101726) in upstream (Fig. 8d). Thus, the velocity of both overland flow and channel flow should be much slower than upstream due to the low topographic gradient and the attenuation effect of forest. As a result, the flood wave contributed by this southwest part of the basin should arrive at the Deep River mouth (Moncure 02102000) later than that from the upstream area, resulting in the bi-peak shape of the flood hydrograph. It is thus reasonable to argue that this bi-peak signature of the flood hydrograph, due to the combined effect of rainfall distribution and spatial heterogeneity of land cover and topography, should have decreased the amplitude of the flood but increased the duration of it.

Fig. 9a shows the nested flood hydrograph from Moncure (02102000) at the Deep River to Kelly (02105769) downstream of the Cape Fear River. The timing difference in the initial rise of the flood hydrograph suggests the control of storm motion from downstream to upstream on flood response. Moreover, the similarity between flood hydrographs at Moncure (02102000) and Lillington (02102500) gives the idea that the bulk of the flood at the latter was contributed by Deep River. Further downstream, the bi-peak feature disappeared and merged into one at Tar Heel (02105500), with a significant difference found between flood hydrographs at Tar Heel (02105500) and Kelly (02105769). This indicates the contribution of the middle CFRB to the Cape Fear River flood downstream.

Along the mainstem of the Cape Fear River from Lillington (02102500) to Kelly (02105769), the unit peak discharges decrease with the increasing VP ratios (Table 5). This decrease in peak discharge is due to the flood plain attenuation effect. A 13% peak discharge attenuation and a 35-h delay of peak timing are observed between Tar Heel (02105500) and Kelly (02105769). This can be attributed to the floodplain storage effect. To analyze this, the net discharge hydrograph was derived by subtracting the observed streamflow at Tar Heel (02105500) from that at Kelly (02105769). As shown in Fig. 9b, during 2000 UTC 14 to 0400 UTC 21 September, a total volume of 177 million m^3 streamflow from upstream was stored in the flood plain between Tar Heel (02105500) and Kelly (02105769). This storage not only has attenuated

the riverine flood from upstream but also has lessened the compound flooding downstream around the Cape Fear River Estuary area. Considering that the volume of the Cape Fear River Estuary is 253 million m^3 (Ensign et al., 2004), the water stored in the flood plain could have flushed out at least 70% of the water in the terminal estuary. Fig. 9c shows the observed total water level and its low-passed filtered component with a cutting off frequency of 40-hour using a Butterworth filter method. The filtered water level represents the component induced by storm surge and riverine input. The storm surge-induced water level peaked around 0430 UTC September 15 at 3.44 m above the mean sea level. After that, the surge retreated. Later, as the river input increased, its impact on the low-frequency water level became dominant. Starting from 0400 UTC September 19, the filtered water level tended to increase again and peaked at 3.44 m around 0142 UTC September 23. However, if there was no timing delay associated with the downstream flood plain, we could expect that the riverine freshwater could have entered the Cape Fear River Estuary days earlier with a larger flood peak. This more significant riverine input could interact with a then higher storm surge to make the compound flooding more devastating. In other words, the downstream flood plain has acted as a buffer between upstream riverine flood and downstream storm surge, which largely attenuated both the riverine flood from upstream but also the compound flooding in the coastal area.

4.3. Drainage network, soil type, and rainfall distribution

As is shown in Fig. 1b, five of the top ten largest unit peak discharges are associated with Florence. Among them, the maximum is found over the Black River at Tomahawk (02106500). With a value of $0.89 \text{ m}^3 \text{s}^{-1} \text{ km}^{-2}$ (Table 5), it is 19% larger than the second maximum ($0.75 \text{ m}^3 \text{s}^{-1} \text{ km}^{-2}$ at 02108000, Table 5) and 35% larger than the previous record set by Fran in 1996. To investigate the exceptional nature of this peak discharge, we put it on the envelope curve developed for the coastal regions below the Fall line in South Carolina, Georgia, and North Carolina by Feaster et al. (2009). As is shown in Fig. 10, the unit peak discharge over the Black River at Tomahawk (02106500) is just below the envelope curve but well above the vast majority of data points of similar basin sizes. Here, we investigate the controller of the exceptional unit discharge by comparing it with that of the second maximum at the NE Cape Fear River basin at Chinquapin (02108000).

It should be noted from Table 5 that both storm total rainfall and

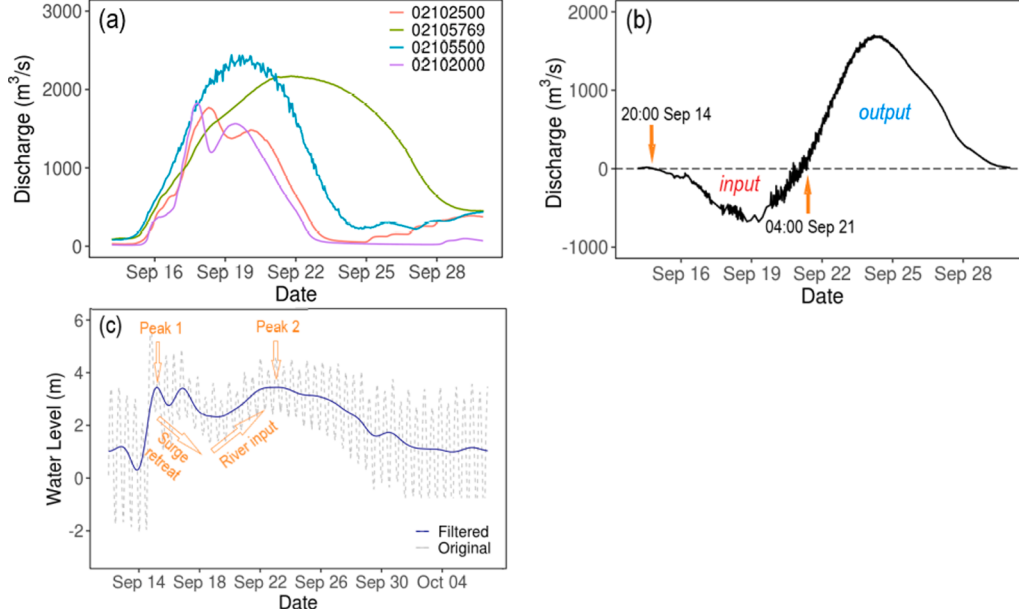


Fig. 9. (a) Nested flood hydrograph at Moncure (02102000, purple), Lillington (02102500, red), Tar Heel (02105500, blue) and Kelly (02105769, green), (b) the net hydrograph derived by subtracting the streamflow at Tar Heel (02105500) from that at Kelly (02105769), (c) Observed low pass filtered (blue solid line) and original (grey dashed line) water level at NOAA tidal gage station 8658120. The locations of gages and details of the drainage network structure are shown in Fig. 2b. (For interpretation of the references to colour in this figure legend, the reader is referred to the web version of this article.)

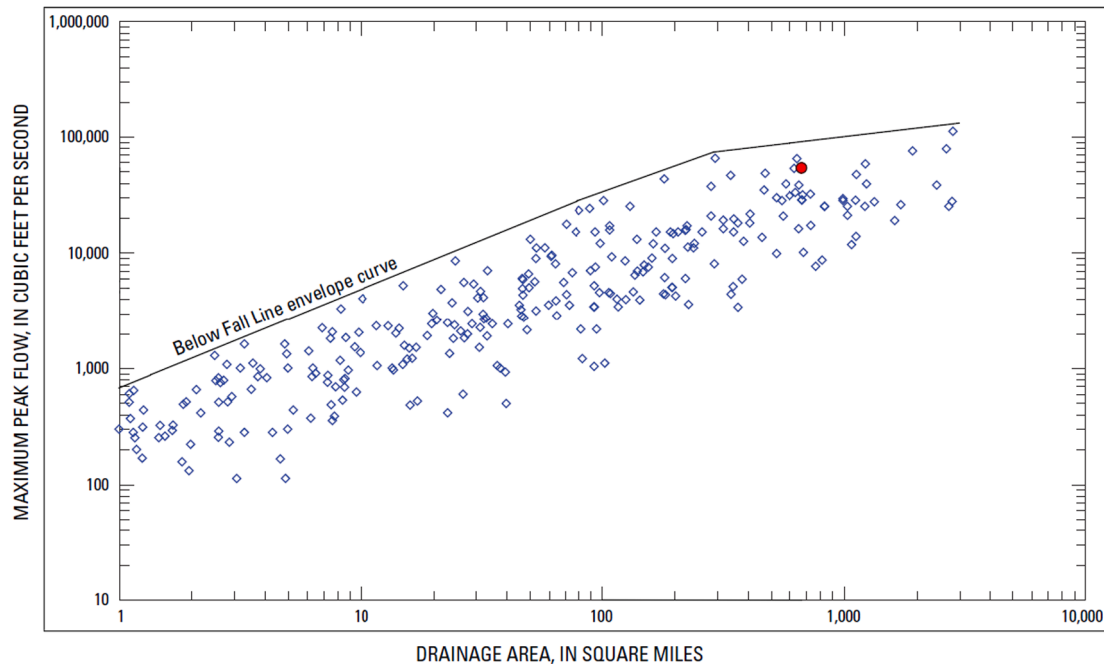


Fig. 10. Envelope curve of peak discharge for streams located below Fall Line in South Carolina, Georgia and North Carolina (Adapted from Fig. 25 in Feaster et al., 2009). The Black River peak discharge during Florence is denoted by the red solid dot. (For interpretation of the references to colour in this figure legend, the reader is referred to the web version of this article.)

runoff depth over Chinquapin (02108000) are higher than that over Tomahawk (02106500). Whereas the drainage area gaged by the former (1551 km^2) is smaller than that by the latter (1751 km^2). This means that the larger unit peak discharge at Tomahawk (02106500) was achieved with less runoff and rainfall over a larger drainage area than that at

Chinquapin (02108000). In addition, the lag time at Chinquapin (02108000) is 13 h shorter than that at Tomahawk (02106500). Moreover, the runoff-to-rainfall ratio is 0.78 at Tomahawk (02106500), which is 10% higher than that at Chinquapin (02108000). We attribute the distinct flood response between the two to their differences in

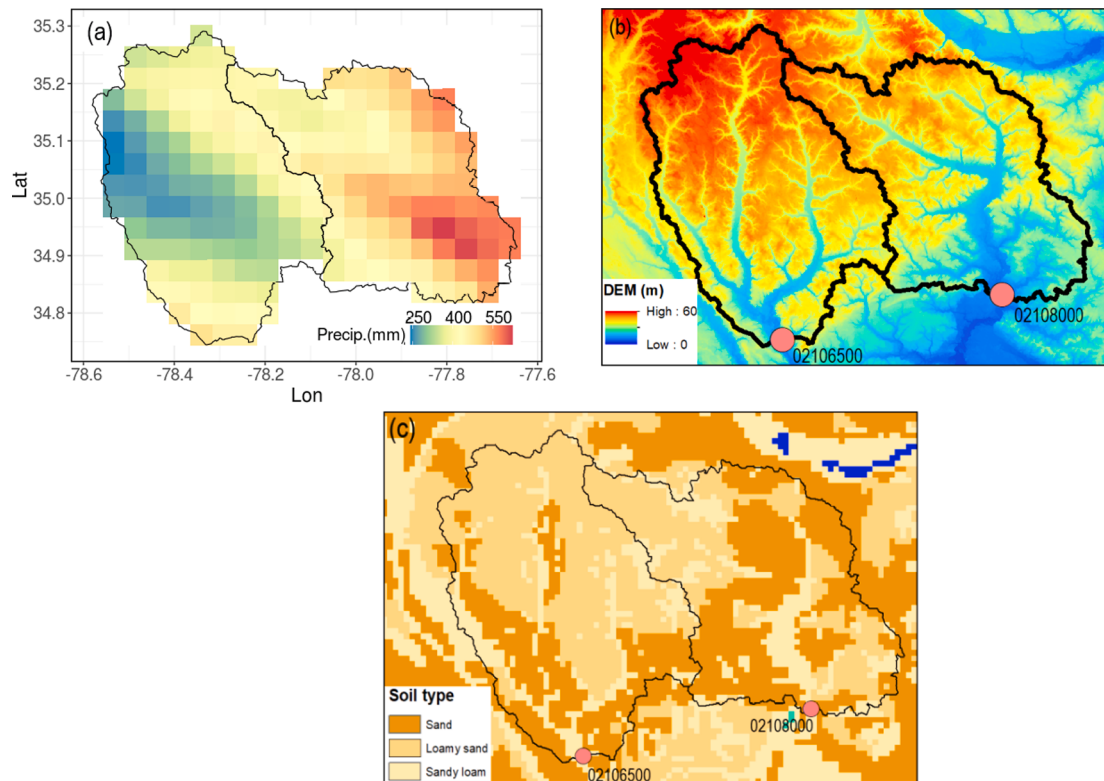


Fig. 11. Storm total rainfall(a), drainage network (b), and soil type (c) over drainage area gaged by Tomahawk (02106500) at Black River and Chinquapin (02108000) at NE Cape Fear River. The drainage areas are outlined with a solid black line. Locations of the gages are also shown.

rainfall distribution, soil type and drainage network.

Fig. 11a shows the distribution of the storm total rainfall over the two basins during Florence. For the Black River basin above Tomahawk (02106500), large portions of rainfall accumulated over the east and northeast part of it. There, the soil type is mainly loamy sand as shown in **Fig. 11c**. Meanwhile, over the NE Cape Fear River basin above Chinquapin (02108000), most of the rainfall was dumped along the east half of the drainage area. The soil type there is primarily sand. As the water storage and hydraulic conductivity of sand are higher than that of loamy sand, a larger amount of water loss to the former should be expected than that to the latter. This difference in water loss can partly explain difference in rainfall-to-runoff ratio of the two basins.

The difference between the two neighboring basins in timing and magnitude of peak discharge is tied to the spatial distribution of rainfall relative to the drainage network. It can be observed from **Fig. 11a** that a considerable portion of rainfall in the Black River basin above Tomahawk (02106500) dropped over the headwater area with lower channel order (larger channel roughness) and longer distance to the outlet. On the contrary, the majority amount of rainfall accumulated near the outlet of the Northeast Cape Fear River basin above Chinquapin (02108000) where the stream order (channel roughness) is high (small). In this case, a faster peak discharge response to rainfall should be expected at Chinquapin (02108000) than that at Tomahawk (02106500). Meanwhile, as it can be observed from **Fig. 11b**, the width of the channel over the most downstream part of the Northeast Cape Fear River basin above Chinquapin (02108000) is much larger than in the Black River basin above Tomahawk (02106500). Moreover, the topography of the former is flatter than the latter. The larger channel width in combination with low topographic gradient is thus the notable feature that explains the smaller peak discharge at Chinquapin (02108000) than that at Tomahawk (02106500).

4.4. Re-infiltration process

Re-infiltration refers to the infiltration of overland flow as it moves downslope towards the channel, which is also known as the “run-on” effect (Corradini et al., 2002, 1998; Nahar et al., 2004). Whereas local infiltration is defined as the amount of water infiltrating into the soil locally from the rainfall. Compared to the latter, re-infiltration normally acts as a secondary process. However, during storm events, re-infiltration can account for more than 50% of total infiltration (Zhang et al., 2020). In addition, the re-infiltration process can significantly decrease the discharge during both rising and falling limbs (Corradini et al., 1998). In this section, we quantify the magnitude of the re-infiltration amount and its effect on streamflow during Florence using WRF-Hydro.

Built upon the Noah land surface model with multi-parameterization options (Noah-MP, Niu et al., 2011), WRF-Hydro enhances the physical realism of the water cycle by integrating subsurface and overland flow routing, base flow, and channel routing via corresponding modules. Among those improvements, the lateral overland routing allows for the consideration of re-infiltration in the model. In this study, a calibrated WRF-Hydro model over the CFRB during Florence was applied. The computational domain has a dimension of 2490 (west to east) × 3490 (north to south) with a 100 m horizontal resolution (**Fig. 2b**), which is 10 times finer than that of Noah-MP. The timestep of Noah-MP is one hour while that of overland and channel routing is 10 s. The precipitation forcing was regredded from the Stage IV multi-sensor rainfall estimation product. Other forcing variables including air temperature, wind, short and longwave radiation, humidity, and pressure were from Phase 2 of the North American Land Data Assimilation System (Mitchell et al., 2004; Xia et al., 2012).

Following Zhang et al. (2020), we calculated the total infiltration, local infiltration, and re-infiltration according to the water balance equation (Eq. (5)). Here, the water storage change refers to the variation of subsurface water. Two numerical experiments were conducted. In the

first experiment (Exp1), lateral routing of surface runoff and the accompanied re-infiltration were simulated. In the second experiment (Exp2), while the lateral movement of the surface was modeled as well, the re-infiltration process during the routing was not simulated. Total infiltration can be calculated as the difference between precipitation input (P, Eq. (5)) and the surface runoff (Runoff, Eq. (5)), which is equal to the sum of simulated water storage change (Dels, Eq. (5)) and evapotranspiration (ET, Eq. (5)) in Exp1. Here, we ignored the amount of surface water that accumulated in the lakes, which were not considered in the model. In the same way, local infiltration was derived by subtracting the simulated runoff (Runoff) in Exp2 from the precipitation (P). Then, the re-infiltration was calculated by subtracting local infiltration from total infiltration.

$$P = ET + Runoff + Dels \quad (5)$$

Table 6 summarizes the simulated water budget with (Exp1) and without (Exp2) considering the re-infiltration process. As shown in **Table 6**, runoff, ET, and Dels represent the accumulative amount during the period of 0000 UTC 14 September to 0000 UTC 12 October 2018 and divided by drainage area. The re-infiltration process is consistently larger than the local infiltration and provides a superior contribution to the infiltration process during Florence. For CFRB and its major sub-basins, the re-infiltration amounts to 76% of the total infiltration on average. In addition, the dominance of the re-infiltration is more pronounced over the upper CFRB than the middle and lower parts. Over Haw River basin above Bynum (02096960) and Deep River basin above Moncure (02102000), the infiltration induced by the re-infiltration process are 90% and 93%, respectively. Meanwhile over the Little River basin above Manchester (02103000), Black River basin above Tomahawk (02106500) and Northeast River basin above Chinquapin (02108000), the refiltration account for 62%, 63%, and 75% of the total infiltration, respectively. We attribute the less significant role of re-infiltration over lower and middle CFRB than the upper part to the larger amount of rainfall the former two parts received. With the torrential precipitation lasting for days, the soil over lower and middle CFRB can get saturated from local infiltration very quickly. Once the soil became saturated, little soil deficit would be available for the re-infiltration process to happen even though overland flow routed laterally. In this case, re-infiltration may take a less important part in total infiltration. Moreover, the re-infiltration process has a significant influence on both the amplitude and timing of the peak discharge. Without considering the re-infiltration effect, simulated peak discharges over the major and sub-basins could arrive 6–17 h earlier, with the amplitudes being 1.3–2.8 times of the observed ones. In this case, the re-infiltration process has largely decreased the peak flood amplitude and delayed its timing.

5. Summary and conclusion

Based on QPEs, rain gage and streamflow observations as well as results from a numerical model, we investigated the flood response of the CFRB during Florence and analyzed the hydrometeorological and hydrologic controls behind it. The main results from this study are summarized as follows:

1. Among Stage IV, NLDAS V2 and MRMS, Stage IV is the “best” product in reproducing the storm total rainfall (mm, KGE = 0.82) and hourly rainfall intensity (mm/h, KGE = 0.77) over the CFRB during Florence.
2. Because of the slow-motion and “L-shaped” track, Florence induced rainfall was much higher in amount than that caused by the other major hurricanes affected CFRB. The resultant storm total rainfall then controlled the runoff depth, unit peak discharge and the shape of flood hydrograph at the basin scale.
3. Hydrologic characteristics exerted influence on flood response at the sub-basin scale. The distinctive bi-peak shape of the flood

Table 6
Simulated water budget with (Exp1) and without (Exp2) overland routing and the associated infiltration amount.

Area	Station	Area mean precipitation (mm)	Runoff (mm)		ET (mm)	Dels (mm)	TotalInfiltration (mm)	LocalInfiltration (mm)	Re-infiltration (mm)	PeakFlow (m ³ /s) Exp1 (Exp2)	PeakDischargeTimingDifference ^b (hour) Exp1-Exp2
			Exp1	Exp2 ^a							
Haw River Deep River	Bynum (02096960) Moncure (02102000)	122 225	64(116) 152(210)	73(62) 91(77)	-15(-56) -18(-62)	58 73	6 5	52 68	1247(3042) 2406(3148)	13 6	
Little River	Manchester (02103000)	269	206(255)	82(62)	-19(-48)	63	24	39	433(1237)	14	
Black River	Tomahawk (02106500)	411	348(388)	67(51)	-4(-28)	63	23	40	1461(2055)	17	
NE CFR	Chinquapin (02108000)	512	460(499)	70(55)	-18(-42)	52	13	39	1826(2711)	12	
Cape Fear River	Kelly (02105769)	283	165(254)	82(68)	36(-39)	118	29	89	3783(5107)	12	

a: Exp1 represents the experiment in which the re-infiltration process is simulated. Exp2 represents the experiment in which only local infiltration is simulated.

b: Peak discharge timing difference indicates the difference of the peak discharge simulated in Exp1 and Exp2. Positive value means that the time for streamflow to peak in Exp1 is later than that in Exp2 and vice versa.

hydrograph at Moncure (02102000) in the Deep River basin was partly due to the spatial heterogeneity of land cover and topographic gradient. The exceptional unit peak discharge at Tomahawk (02106500) was associated with the small width of its channel network, relatively steep topographic gradient, and rainfall distribution. In addition, the coastal flood plain has acted as a buffer between upstream riverine flood and downstream storm surge, which caused a 13% peak discharge attenuation and a 35-h delay of peak timing.

4. Numerical experiments suggest that re-infiltration was superior to local infiltration over CFRB during Florence. For major and sub-river basins, re-infiltration accounted for 76% of the total infiltration on average. Without the re-infiltration effect, the peak discharge could be 1.3–2.8 times of observed ones and arrive 6–17 h earlier.

In summary, the results achieved here show that the slow-motion in combination to the “L-shaped” track was the most distinctive feature of Florence that resulted in the catastrophic rainfall and flooding all over the CFRB. At the basin scale, the flood response strongly depends on the storm total rainfall instead of rainfall intensity. This finding aligns with Hewlett et al. (1977), but differs from the case of Puerto Rico during Hurricane Georges, where the flood response was highly controlled by peak rainfall rates (Smith et al., 2005). Such difference should be due to the faster response of Puerto Rico watershed than CFRB, which is tied to their difference in topographic gradients. At sub-basin scales, in consistent with what is reported by previous studies (Lininger and Latrubesse, 2016; Sturdevant-Rees et al., 2001; Zhang et al., 2001), land use, soil type, coastal flood plain storage as well as the river network could exert secondary important influence on flood response. Re-infiltration process, similar with that reported by Zhang et al. (2020), was superior to local infiltration. However, due to the limited observation data availability, human activity’s effect (e.g., dams and reservoirs) on the flood response was not covered in this study. In addition, the influence of initial soil moisture on flood response, as reported by previous studies (Grillakis et al., 2016; Li et al., 2020; Nikolopoulos et al., 2011; Uber et al., 2018), can also be significant. Our study points out the important role that coastal flood plain played in attenuating the compound flooding. Modeling efforts may be further refined by incorporating the coastal flood plain and its influence on compound flooding potential during hurricane events through coupled hydrologic-hydrodynamic simulations (Kumbier et al., 2018; Santiago-Collazo et al., 2019; Yin et al., 2021).

CRediT authorship contribution statement

Dongxiao Yin: Writing – original draft, Visualization, Investigation, Methodology, Software, Validation. **Z. George Xue:** Writing – review & editing, Project administration, Funding acquisition, Supervision, Conceptualization. **John C. Warner:** Project administration, Funding acquisition, Supervision, Conceptualization. **Daoyang Bao:** Visualization, Methodology, Software, Validation. **Yongjie Huang:** Software, Methodology. **Wei Yu:** Software, Methodology.

Declaration of Competing Interest

The authors declare that they have no known competing financial interests or personal relationships that could have appeared to influence the work reported in this paper.

Acknowledgements

This research is funded by USGS The Cooperative Ecosystem Studies Units (award# G20AC00099). Dongxiao Yin is also supported by the Economic Development Assistantship program at LSU. Computation resources and supports from LSU High Performance Computing is appreciated. We thank Evette Williams for proofreading the article.

Appendix A. Supplementary data

Supplementary data to this article can be found online at <https://doi.org/10.1016/j.jhydrol.2021.127139>.

References

- Callaghan, J., 2020. Extreme rainfall and flooding from Hurricane Florence. *Trop. Cyclone Res. Rev.* 9, 172–177. <https://doi.org/10.1016/j.tcr.2020.07.002>.
- Cánovas-García, F., García-Galiano, S., Alonso-Sarriá, F., 2018. Assessment of satellite and radar quantitative precipitation estimates for real time monitoring of meteorological extremes over the southeast of the Iberian Peninsula. *Remote Sens.* 10, 1023. <https://doi.org/10.3390/rs10071023>.
- Chen, X., Kumar, M., McGlynn, B.L., 2015. Variations in streamflow response to large hurricane-season storms in a southeastern U.S. watershed. *J. Hydrometeorol.* 16, 55–69. <https://doi.org/10.1175/JHM-D-14-0044.1>.
- Corradini, C., Govindaraju, R.S., Morbidelli, R., 2002. Simplified modelling of areal average infiltration in the hillslope scale. *Hydrolog. Process.* 16, 1757–1770. <https://doi.org/10.1002/hyp.394>.
- Corradini, C., Morbidelli, R., Melone, F., 1998. On the interaction between infiltration and Hortonian runoff. *J. Hydrol.* 204, 52–67. [https://doi.org/10.1016/S0022-1694\(97\)00100-5](https://doi.org/10.1016/S0022-1694(97)00100-5).
- Curts Weaver, B.J., Pope Raleigh, B.F., Carolina, N., 2001. Low-Flow Characteristics and Discharge Profiles for Selected Streams in the Cape Fear River Basin, North Carolina, through 1998.
- Ensign, S.H., Halls, J.N., Mallin, M.A., 2004. Application of digital bathymetry data in an analysis of flushing times of two large estuaries. *Comput. Geosci.* 30, 501–511. <https://doi.org/10.1016/j.cageo.2004.03.015>.
- Feaster, T.D., Gotvald, A.J., Weaver, J.C., 2009. Magnitude and Frequency of Rural Floods in the Southeastern United States, 2006; Volume 3, South Carolina.
- Feaster, T.D., Weaver, J.C., Gotvald, A.J., Kolb, K.R., 2018. Preliminary peak stage and streamflow data for selected U.S. Geological Survey streamgaging stations in North and South Carolina for flooding following Hurricane Florence, September 2018. *Open-File Rep.* 2018-1172. <https://doi.org/10.3133/ofr20181172>.
- Gharamti, M.E., McCreight, J.L., Noh, S.J., Hoar, T.J., Rafieeinabas, A., Johnson, B.K., 2021. Ensemble streamflow data assimilation using WRF-Hydro and DART: novel localization and inflation techniques applied to Hurricane Florence flooding. *Hydrolog. Earth Syst. Sci.* 25, 5315–5336. <https://doi.org/10.5194/hess-25-5315-2021>.
- Gochis, D., Barlage, M., Cabell, R., Casali, M., Dugger, A., Fitzgerald, K., McAllister, M., McCreight, J., Rafieeinabas, A., Read, L., Sampson, K., Yates, D., Zhang, Y., 2020. The WRF-Hydro modeling system technical description, (Version 5.1.1), NCAR Technical Note.
- Gori, A., Lin, N., Smith, J., 2020. Assessing compound flooding from landfalling tropical cyclones on the North Carolina Coast. *Water Resour. Res.* 56 <https://doi.org/10.1029/2019WR026788>.
- Griffin, M., Malsick, M., Mizell, H., Moore, L., 2020. Historic rainfall and record-breaking flooding from hurricane florence in the Pee Dee Watershed. *J. South Carolina Water Resour.* 6, 28–35. <https://doi.org/10.34068/jscwr.06.03>.
- Grillakis, M.G., Koutoulis, A.G., Komma, J., Tsanis, I.K., Wagner, W., Blöschl, G., 2016. Initial soil moisture effects on flash flood generation – a comparison between basins of contrasting hydro-climatic conditions. *J. Hydrol.* 541, 206–217. <https://doi.org/10.1016/j.jhydrol.2016.03.007>.
- Gupta, H.V., Kling, H., Yilmaz, K.K., Martinez, G.F., 2009. Decomposition of the mean squared error and NSE performance criteria: implications for improving hydrological modelling. *J. Hydrol.* 377, 80–91. <https://doi.org/10.1016/j.jhydrol.2009.08.003>.
- Hewlett, J.D., Fortson, J.C., Cunningham, G.B., 1977. The effect of rainfall intensity on storm flow and peak discharge from forest land. *Water Resour. Res.* 13, 259–266. <https://doi.org/10.1029/WR013i002p00259>.
- Huang, J.C., Yu, C.K., Lee, J.Y., Cheng, L.W., Lee, T.Y., Kao, S.J., 2012. Linking typhoon tracks and spatial rainfall patterns for improving flood lead time predictions over a mesoscale mountainous watershed. *Water Resour. Res.* 48, 1–15. <https://doi.org/10.1029/2011WR011508>.
- Hultquist, C., Cervone, G., 2020. Integration of crowdsourced images, USGS networks, remote sensing, and a model to assess flood depth during Hurricane Florence. *Remote Sens.* 12, 834. <https://doi.org/10.3390/rs12050834>.
- Jiang, H., Ramirez, E.M., Cecil, D.J., 2013. Convective and rainfall properties of tropical cyclone inner cores and rainbands from 11 years of TRMM data. *Mon. Weather Rev.* 141, 431–450. <https://doi.org/10.1175/MWR-D-11-00360.1>.
- Kumbier, K., Carvalho, R.C., Vafeidis, A.T., Woodroffe, C.D., 2018. Investigating compound flooding in an estuary using hydrodynamic modelling: a case study from the Shoalhaven River, Australia. *Nat. Hazards Earth Syst. Sci.* 18, 463–477. <https://doi.org/10.5194/nhess-18-463-2018>.
- Kunkel, K.E., Champion, S.M., 2019. An assessment of rainfall from hurricanes Harvey and Florence relative to other extremely wet storms in the United States. *Geophys. Res. Lett.* 46, 13500–13506. <https://doi.org/10.1029/2019GL085034>.
- Li, X., Zhao, G., Nielsen-Gammon, J., Salazar, J., Wigmosta, M., Sun, N., Judi, D., Gao, H., 2020. Impacts of urbanization, antecedent rainfall event, and cyclone tracks on extreme floods at Houston reservoirs during Hurricane Harvey. *Environ. Res. Lett.* 15, 124012. <https://doi.org/10.1088/1748-9326/abc4ff>.
- Lin, Y., 2011. GCIP/EOP Surface: Precipitation NCEP/EMC 4KM Gridded Data (GRIB) Stage IV Data. Version 1.0. <https://doi.org/https://doi.org/10.5065/D6PG1QDD>.
- Lininger, K.B., Latrubesse, E.M., 2016. Flooding hydrology and peak discharge attenuation along the middle Araguaia River in central Brazil. *Catena* 143, 90–101. <https://doi.org/10.1016/j.catena.2016.03.043>.
- Miller, D.A., White, R.A., 1998. A Conterminous United States Multilayer Soil Characteristics Dataset for Regional Climate and Hydrology Modeling. *Earth Interact.* 2, 2–2. [https://doi.org/10.1175/1087-3562\(1998\)002<0002:cusms>2.0.co;2](https://doi.org/10.1175/1087-3562(1998)002<0002:cusms>2.0.co;2).
- Mitchell, K.E., Lohmann, D., Houser, P.R., Wood, E.F., Schaake, J.C., Robock, A., Cosgrove, B.A., Sheffield, J., Duan, Q., Luo, L., Higgins, R.W., Pinker, R.T., Tarpley, J.D., Lettenmaier, D.P., Marshall, C.H., Entin, J.K., Pan, M., Shi, W., Koren, V., Meng, J., Ramsay, B.H., Bailey, A.A., 2004. The multi-institution North American Land Data Assimilation System (NLDAS): Utilizing multiple GCIP products and partners in a continental distributed hydrological modeling system. *J. Geophys. Res. D Atmos.* 109, 1–32. <https://doi.org/10.1029/2003jd003823>.
- N.C. Department of Environmental Quality Division of Water Resources, 2016. Cape Fear River Surface Water Supply Evaluation.
- Nahar, N., Govindaraju, R.S., Corradini, C., Morbidelli, R., 2004. Role of run-on for describing field-scale infiltration and overland flow over spatially variable soils. *J. Hydrol.* 286, 36–51. <https://doi.org/10.1016/j.jhydrol.2003.09.011>.
- Nikolopoulos, E.I., Anagnostou, E.N., Borga, M., Vivoni, E.R., Papadopoulos, A., 2011. Sensitivity of a mountain basin flash flood to initial wetness condition and rainfall variability. *J. Hydrol.* 402, 165–178. <https://doi.org/10.1016/j.jhydrol.2010.12.020>.
- Niu, G.Y., Yang, Z.L., Mitchell, K.E., Chen, F., Ek, M.B., Barlage, M., Kumar, A., Manning, K., Niyogi, D., Rosero, E., Tewari, M., Xia, Y., 2011. The community Noah land surface model with multiparameterization options (Noah-MP): 1. Model description and evaluation with local-scale measurements. *J. Geophys. Res. Atmos.* 116, 1–19. <https://doi.org/10.1029/2010JD015139>.
- Paerl, H.W., Hall, N.S., Hounshell, A.G., Luetkett, R.A., Rossignol, K.L., Osburn, C.L., Bales, J., 2019. Recent increase in catastrophic tropical cyclone flooding in coastal North Carolina, USA: long-term observations suggest a regime shift. *Sci. Rep.* 9 <https://doi.org/10.1038/s41598-019-46928-9>.
- Rappaport, E.N., 2014. Fatalities in the United States from Atlantic tropical cyclones: new data and interpretation. *Bull. Am. Meteorol. Soc.* 95, 341–346. <https://doi.org/10.1175/BAMS-D-12-00074.1>.
- Santiago-Collazo, F.L., Bilskie, M.V., Hagen, S.C., 2019. A comprehensive review of compound inundation models in low-gradient coastal watersheds. *Environ. Model. Softw.* 119, 166–181. <https://doi.org/10.1016/j.envsoft.2019.06.002>.
- Smith, J.A., Baeck, M.L., Morrison, J.E., Sturdevant-Rees, P., 2000. Catastrophic rainfall and flooding in Texas. *J. Hydrometeorol.* 1, 5–25. [https://doi.org/10.1175/1525-7541\(2000\)001<0005:CRAFIT>2.0.CO;2](https://doi.org/10.1175/1525-7541(2000)001<0005:CRAFIT>2.0.CO;2).
- Smith, J.A., Baeck, M.L., Villarini, G., Krajewski, W.F., 2010. The hydrology and hydrometeorology of flooding in the Delaware River basin. *J. Hydrometeorol.* 11, 841–859. <https://doi.org/10.1175/2010JHM1236.1>.
- Smith, J.A., Sturdevant-Rees, P., Baeck, M.L., Larsen, M.C., 2005. Tropical cyclones and the flood hydrology of Puerto Rico. *Water Resour. Res.* 41, 1–16. <https://doi.org/10.1029/2004WR003530>.
- Sturdevant-Rees, P., Smith, J.A., Morrison, J., Baeck, M.L., 2001. Tropical storms and the flood hydrology of the central Appalachians. *Water Resour. Res.* 37, 2143–2168. <https://doi.org/10.1029/2000WR900310>.
- Thiemig, V., Rojas, R., Zambrano-Bigiarini, M., Levizzani, V., De Roo, A., 2012. Validation of satellite-based precipitation products over sparsely Gauged African River basins. *J. Hydrometeorol.* 13, 1760–1783. <https://doi.org/10.1175/JHM-D-12-032.1>.
- Uber, M., Vandervaere, J.-P., Zin, I., Braud, I., Heistermann, M., Legout, C., Molinié, G., Nord, G., 2018. How does initial soil moisture influence the hydrological response? A case study from southern France. *Hydrol. Earth Syst. Sci.* 22, 6127–6146. <https://doi.org/10.5194/hess-22-6127-2018>.
- Villarini, G., Goska, R., Smith, J.A., Vecchi, G.A., 2014. North atlantic tropical cyclones and U.S. flooding. *Bull. Am. Meteorol. Soc.* 95, 1381–1388. <https://doi.org/10.1175/BAMS-D-13-0060.1>.
- Villarini, G., Smith, J.A., 2010. Flood peak distributions for the eastern United States. *Water Resour. Res.* 46 <https://doi.org/10.1029/2009WR008395>.
- Villarini, G., Smith, J.A., Baeck, M.L., Marchok, T., Vecchi, G.A., 2011. Characterization of rainfall distribution and flooding associated with U.S. landfalling tropical cyclones: Analyses of Hurricanes Frances, Ivan, and Jeanne (2004). *J. Geophys. Res. Atmos.* 116. <https://doi.org/10.1029/2011JD016175>.
- Weaver, J.C., Carolina, N., 1997. Low-Flow Characteristics and Profiles for the Deep River in the Cape Fear River Basin, North Carolina.
- Williams, T.M., Hitchcock, D., Song, B., O'Halloran, T., 2020. Hurricane florence flooding in Georgetown County: a qualitative explanation of the interactions of estuary and tidal river. *J. South Carolina Water Resour.* 6, 36–45. <https://doi.org/10.34068/jscwr.06.04>.
- Xia, Y., Mitchell, K., Ek, M., Sheffield, J., Cosgrove, B., Wood, E., Luo, L., Alonge, C., Wei, H., Meng, J., Livneh, B., Lettenmaier, D., Koren, V., Duan, Q., Mo, K., Fan, Y., Mocko, D., 2012. Continental-scale water and energy flux analysis and validation for the North American Land Data Assimilation System project phase 2 (NLDAS-2): 1. Intercomparison and application of model products. *J. Geophys. Res. Atmos.* 117. <https://doi.org/10.1029/2011JD016048>.
- Yin, D., Muñoz, D.F., Bakhtyar, R., Xue, Z.G., Moftakhar, H., Ferreira, C., Mandli, K., 2021. Extreme water level simulation and component analysis in delaware estuary during hurricane Isabel. *JAWRA J. Am. Water Resour. Assoc.* <https://doi.org/10.1111/1752-1688.12947>.
- Zambon, J.B., He, R., Warner, J.C., Hegermiller, C.A., 2021. Impact of SST and surface waves on hurricane Florence (2018): a coupled modeling investigation. *Weather Forecast.* 1713–1734 <https://doi.org/10.1175/waf-d-20-0171.1>.
- Zambrano-Bigiarini, M., Nauditt, A., Birkel, C., Verbiest, K., Ribbe, L., 2017. Temporal and spatial evaluation of satellite-based rainfall estimates across the complex

- topographical and climatic gradients of Chile. *Hydrol. Earth Syst. Sci.* 21, 1295–1320. <https://doi.org/10.5194/hess-21-1295-2017>.
- Zhang, J., Howard, K., Langston, C., Kaney, B., Qi, Y., Tang, L., Grams, H., Wang, Y., Cockcks, S., Martinaitis, S., Arthur, A., Cooper, K., Brogden, J., Kitzmiller, D., 2016. Multi-Radar Multi-Sensor (MRMS) quantitative precipitation estimation: Initial operating capabilities. *Bull. Am. Meteorol. Soc.* 97, 621–638. <https://doi.org/10.1175/BAMS-D-14-00174.1>.
- Zhang, J., Lin, P., Gao, S., Fang, Z., 2020. Understanding the re-infiltration process to simulating streamflow in North Central Texas using the WRF-hydro modeling system. *J. Hydrol.* 587, 124902. <https://doi.org/10.1016/j.jhydrol.2020.124902>.
- Zhang, W., Villarini, G., Vecchi, G.A., Smith, J.A., 2018. Urbanization exacerbated the rainfall and flooding caused by hurricane Harvey in Houston. *Nature* 563, 384–388. <https://doi.org/10.1038/s41586-018-0676-z>.
- Zhang, Y., Smith, J.A., Baeck, M.L., 2001. The hydrology and hydrometeorology of extreme floods in the Great Plains of Eastern Nebraska. *Adv. Water Resour.* 24, 1037–1049. [https://doi.org/10.1016/S0309-1708\(01\)00037-9](https://doi.org/10.1016/S0309-1708(01)00037-9).